nature biotechnology

SUPPLEMENTARY INFORMATION

https://doi.org/10.1038/s41587-019-0321-x

In the format provided by the authors and unedited.

A laser-engraved wearable sensor for sensitive detection of uric acid and tyrosine in sweat

Yiran Yang[1,7], Yu Song[1,2,7], Xiangjie Bo[1,7], Jihong Min[1], On Shun Pak[3], Lailai Zhu[4], Minqiang Wang[1], Jiaobing Tu[1], Adam Kogan[1], Haixia Zhang[2], Tzung K. Hsiai[5], Zhaoping Li[6] and Wei Gao[1]*

---

[1]Andrew and Peggy Cherng Department of Medical Engineering, California Institute of Technology, Pasadena, CA, USA. [2]National Key Lab of Micro/Nano Fabrication Technology, Peking University, Beijing, China. [3]Department of Mechanical Engineering, Santa Clara University, Santa Clara, CA, USA. [4]Department of Mechanical and Aerospace Engineering, Princeton University, Princeton, NJ, USA. [5]Division of Cardiology, Department of Medicine, David Geffen School of Medicine, University of California, Los Angeles, CA, USA. [6]Division of Clinical Nutrition, Department of Medicine, David Geffen School of Medicine, University of California, Los Angeles, CA, USA. [7]These authors contributed equally: Yiran Yang, Yu Song, Xiangjie Bo.
*e-mail: weigao@caltech.edu

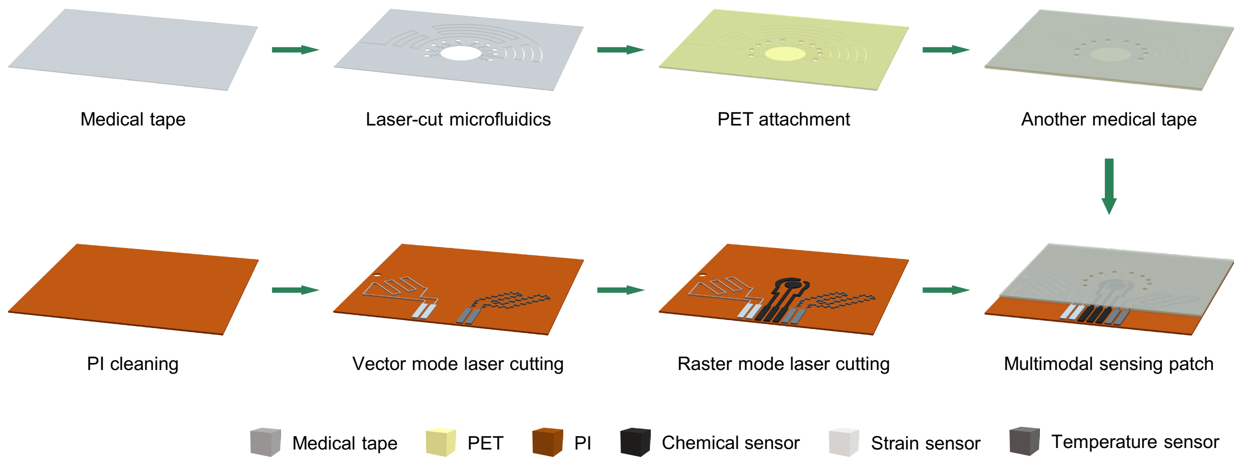

Supplementary Fig. 1. Fabrication process of the laser-enabled patch.

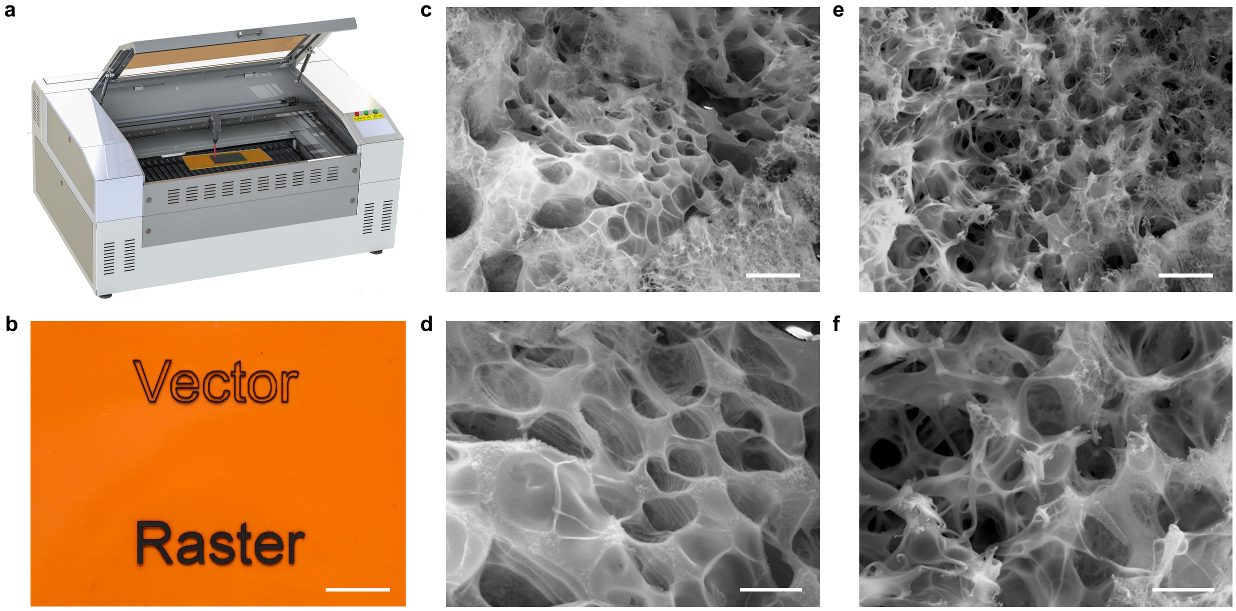

Supplementary Fig. 2. Vector and raster modes of the laser cutting process. a, A CO_2 laser cutting machine. **b**, Optical image of laser-scribed graphene patterns via vector mode and raster mode, respectively. Scale bar, 1 cm. **c**,**d**, SEM images of vector mode-scribed graphene structure. Scale bars represent 5 µm (**c**) and 2 µm (**d**), respectively. **e**,**f**, SEM images of raster mode-scribed graphene structure. Scale bars represent 5 µm (**e**) and 2 µm (**f**), respectively.

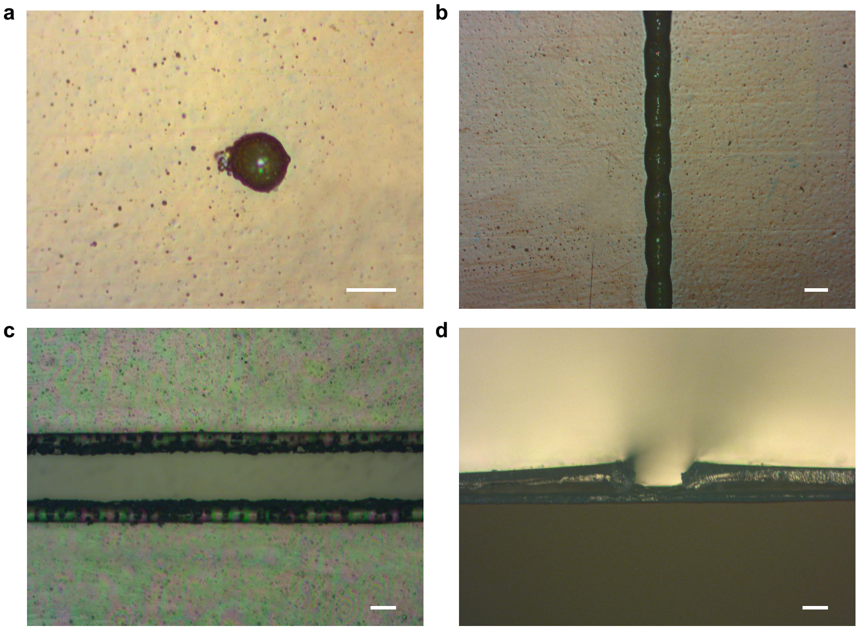

Supplementary Fig. 3. Microscopic images showing the resolution of the laser engraving. a–d, a graphene microelectrode fabricated by the raster mode (**a**), a graphene micropattern fabricated by vector mode (**b**), and a microfluidic channel fabricated by vector mode under top view (**c**) and cross-sectional view (**d**). Scale bars, 100 μm.

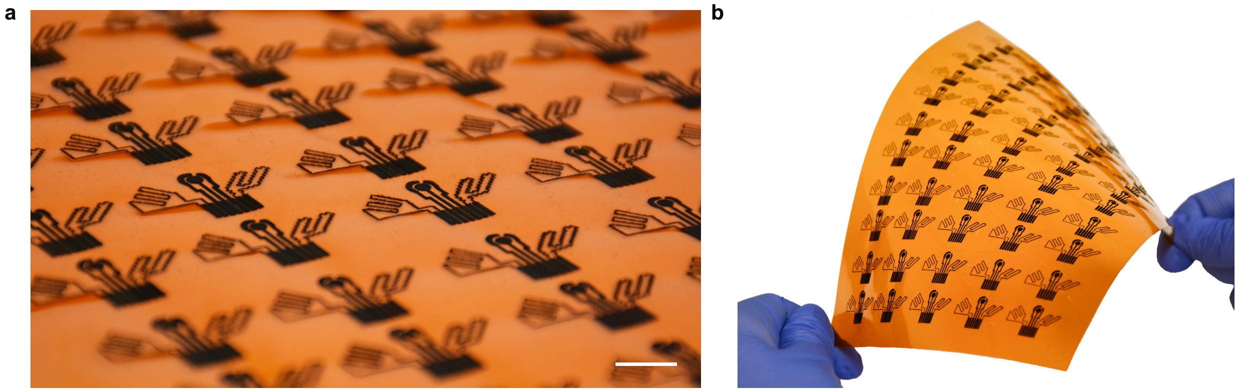

Supplementary Fig. 4. Low-cost and mass-production of the flexible multimodal sensor arrays. Scale bar, 1 cm.

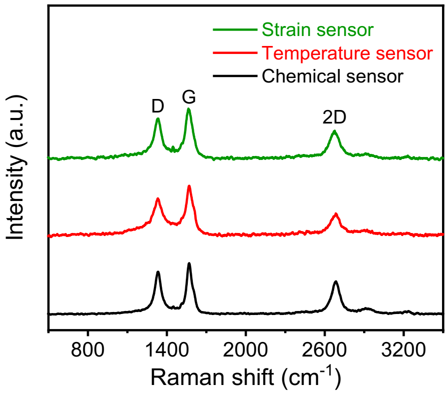

Supplementary Fig. 5. Characterization of the LEG-based chemical, temperature, and strain sensors using Raman spectroscopy. Three experiments were performed independently with similar results.

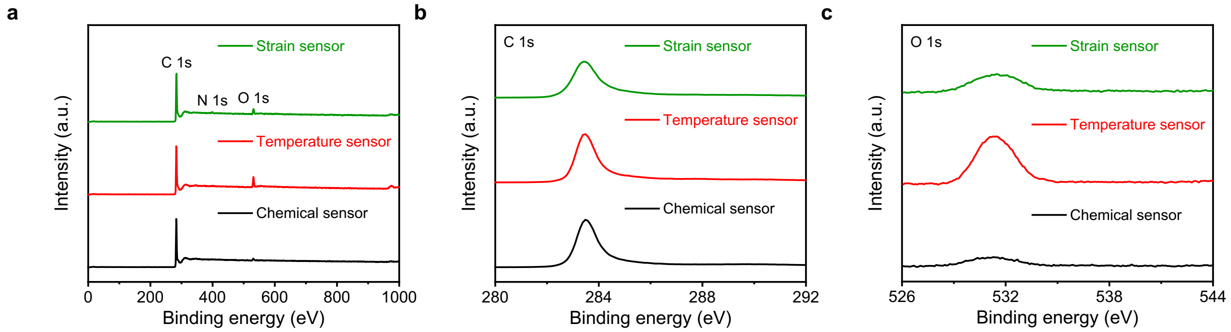

Supplementary Fig. 6. Characterization of the LEG-based chemical, temperature, and strain sensors using X-ray photoelectron spectroscopy (XPS). Three experiments were performed independently with similar results.

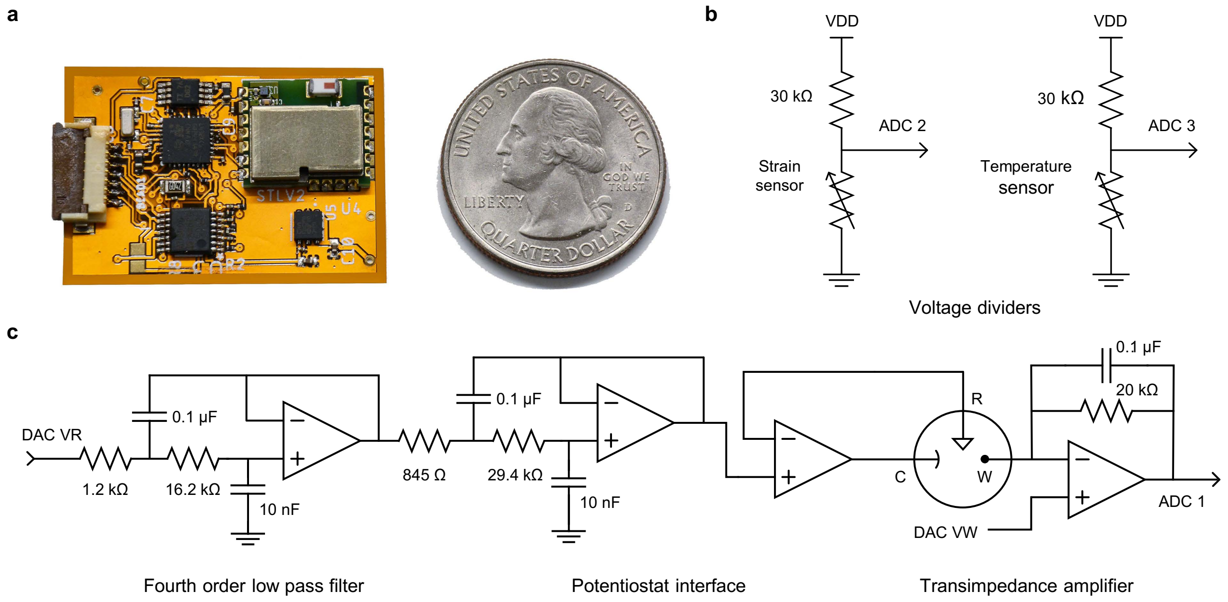

Supplementary Fig. 7. Circuit diagram of the multiplexed sensing system. a, An FPCB next to a quarter dollar coin. **b**, Circuit diagram of the voltage dividers for driving physical sensor measurements. **c**, Circuit diagram of analog front-end potentiostat for voltammetric sensing. VR and VW correspond to the reference potential and the working potential, respectively.

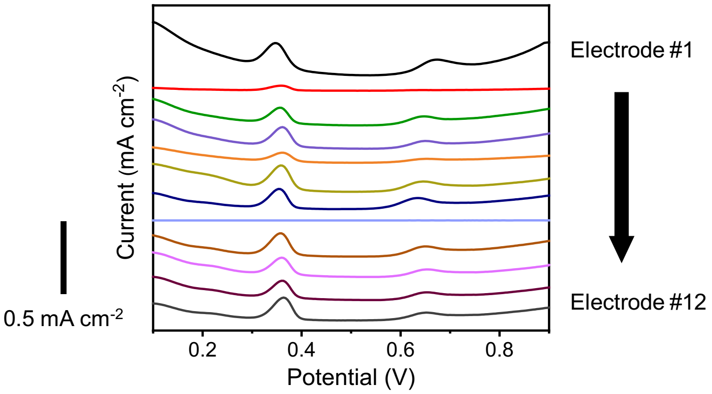

Supplementary Fig. 8. Optimization of the LEG-based chemical sensor under different laser parameters. Condition, 50 μM UA and 50 μM Tyr. Five experiments were performed independently with similar results.

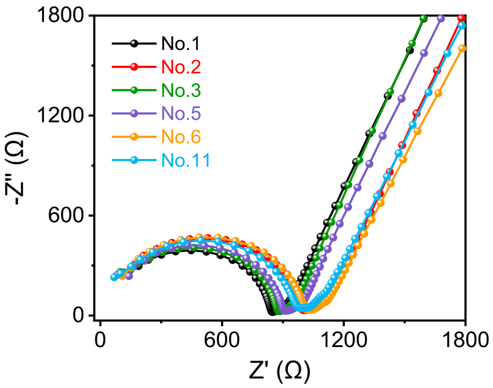

Supplementary Fig. 9. Electrochemical impedance spectroscopy (EIS) for LEG-based electrodes prepared with different laser-engraving parameters. EIS tests were performed in a solution containing 0.2 M KCl and 5 mM $[Fe(CN)_6]^{3-}$ at open circuit potentials with an AC amplitude of 5 mV in the range of 0.1–1000000 Hz. All conditions were tested for once at the same time.

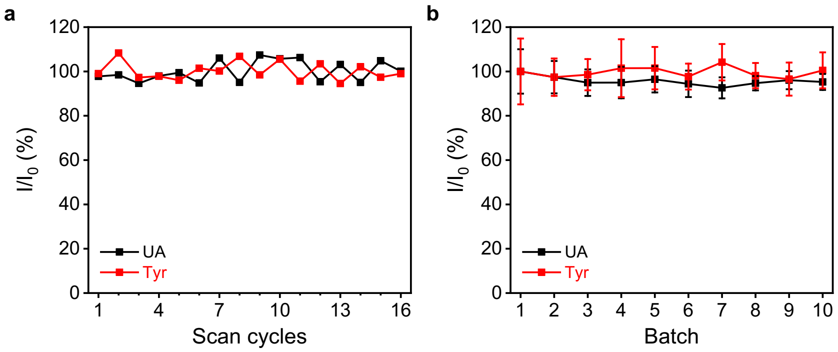

Supplementary Fig. 10. Reproducibility of the LEG-based chemical sensors for Tyr and UA sensing. a, Continuous successive detection of UA and Tyr using an LEG-CS for 16 cycles. I and I_0 represent the peak amplitudes of the DPV plot obtained from a give scan cycle and the first cycle, respectively. **b**, Batch to batch variation of the LEG-based chemical sensor performance (10 batches). I and I_0 represent the peak amplitude of the DPV plot, and the average peak amplitude obtained from the first batch, respectively. Measure of the centre is the mean value of each batch. Error bars represent the standard deviations of the peak amplitudes measured from 16 sensors. Conditions: 50 and 100 μM of UA and Tyr.

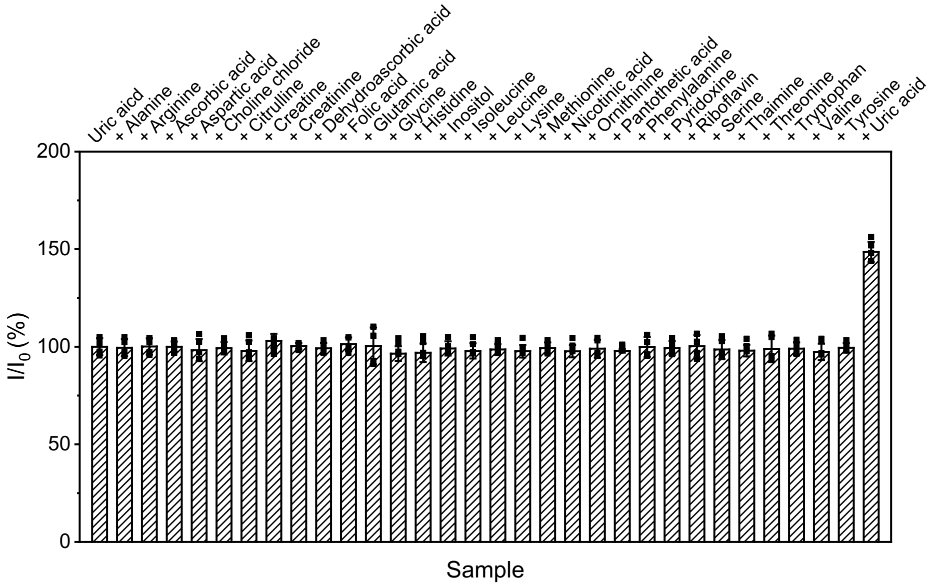

Supplementary Fig. 11. The selectivity of the LEG-CS to UA over other analytes in human sweat. I and I_0 represent the peak amplitude of the DPV plot of an LEG-CS, and the average peak amplitude obtained from the initial UA solution, respectively. The concentrations of the initial UA and other analytes are based on **Supplementary Table 2**. UA concentration was increased by 50% in the end. Error bars represent the standard deviations of 4 independent measurements; measure of the centre is the mean of the 4 independent measurements.

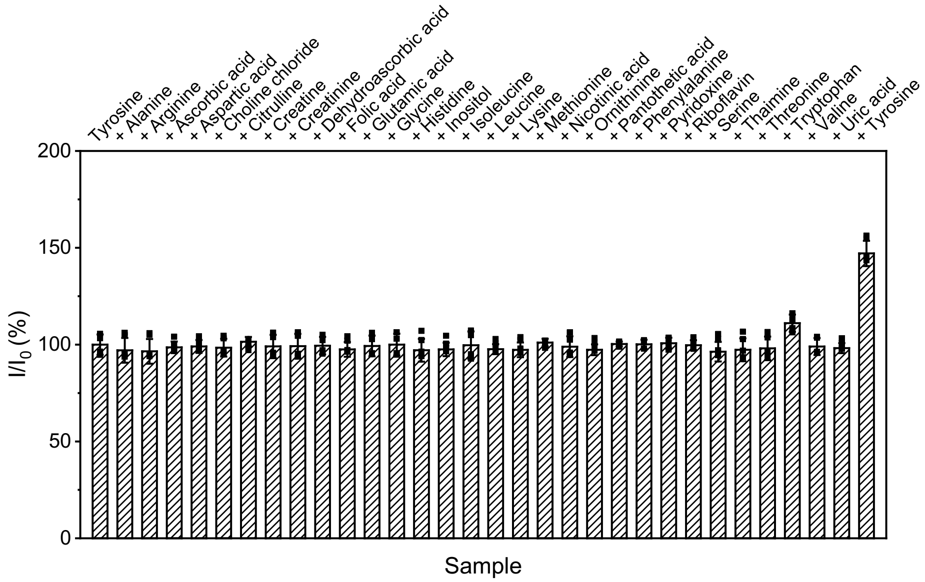

Supplementary Fig. 12. The selectivity of the LEG-CS to Tyr over other analytes in human sweat. I and I_0 represent the peak amplitude of the DPV plot of an LEG-CS, and the average peak amplitude obtained from the initial Tyr solution, respectively. The concentrations of the initial Tyr and other analytes are based on **Supplementary Table 2**. Tyr concentration was increased by 50% in the end. Error bars represent the standard deviations of four measurements. Error bars represent the standard deviations of 4 independent measurements; measure of the centre is the mean of the 4 independent measurements.

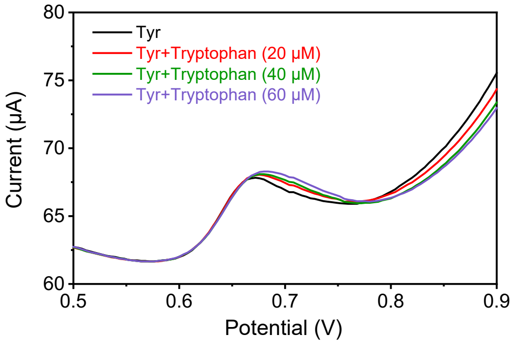

Supplementary Fig. 13. The selectivity of the LEG-CS to Tyr over tryptophan. The DPV plots were obtained from solutions containing physiologically relevant levels of Tyr (170 μM) and tryptophan (20, 40 and 60 μM). The experiment was repeated 5 times independently with similar results.

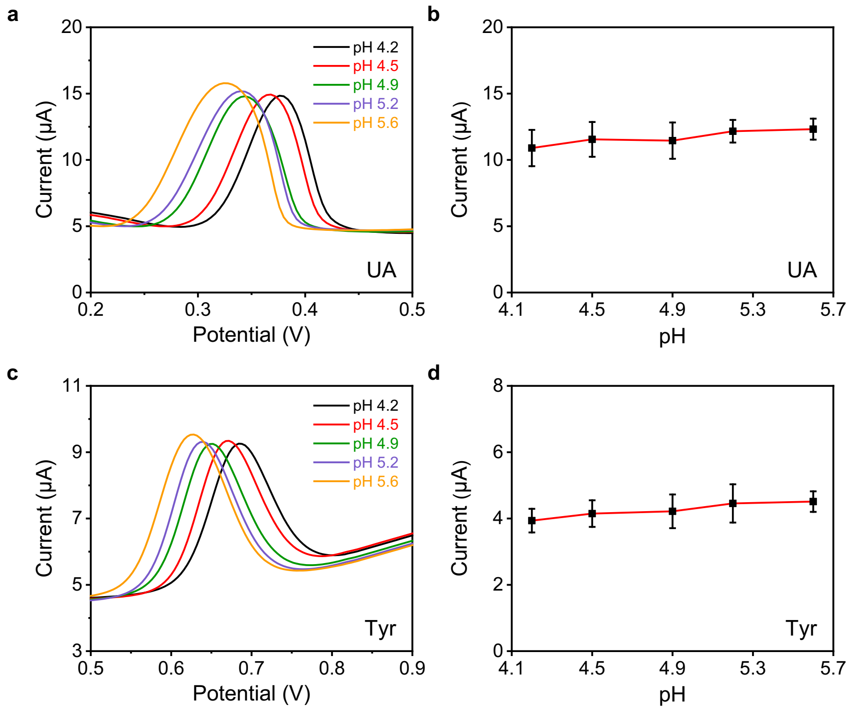

Supplementary Fig. 14. The dependence of sensor response on the solution pH levels. **a**,**b**, The DPV responses (**a**) and the corresponding peak amplitudes (**b**) of the LEG-based chemical sensors (3 mm in diameter) for UA sensing in solutions with different pHs. **c**,**d**, The DPV responses (**c**) and the corresponding peak amplitudes (**d**) of the LEG-based chemical sensors for Tyr sensing in solutions with different pHs. To prepare the artificial sweat samples with different pH, lactic acid was used to adjust the pH of the PBS buffer (0.3X) solutions to physiologically relevant pHs. The UA and Tyr concentrations are 100 and 100 μM, respectively. Throughout the figure, five independent experiments were performed with similar results, and the mean values were taken as measure of the centre. Error bars represent the standard deviations of measurements from 5 sensors.

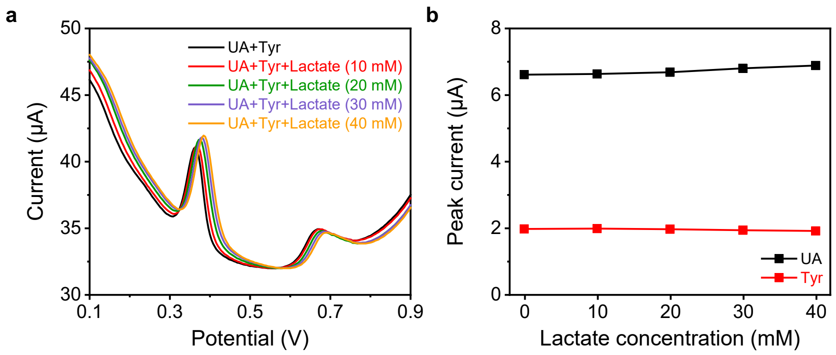

Supplementary Fig. 15. The selectivity of the LEG-CS to lactate. Physiologically relevant levels of lactic acid (10, 20, 30, and 40 mM) were added to 0.1 M ABS (pH 4.6) containing 50 µM UA and 50 µM Tyr. The experiment was repeated 5 times independently with similar results.

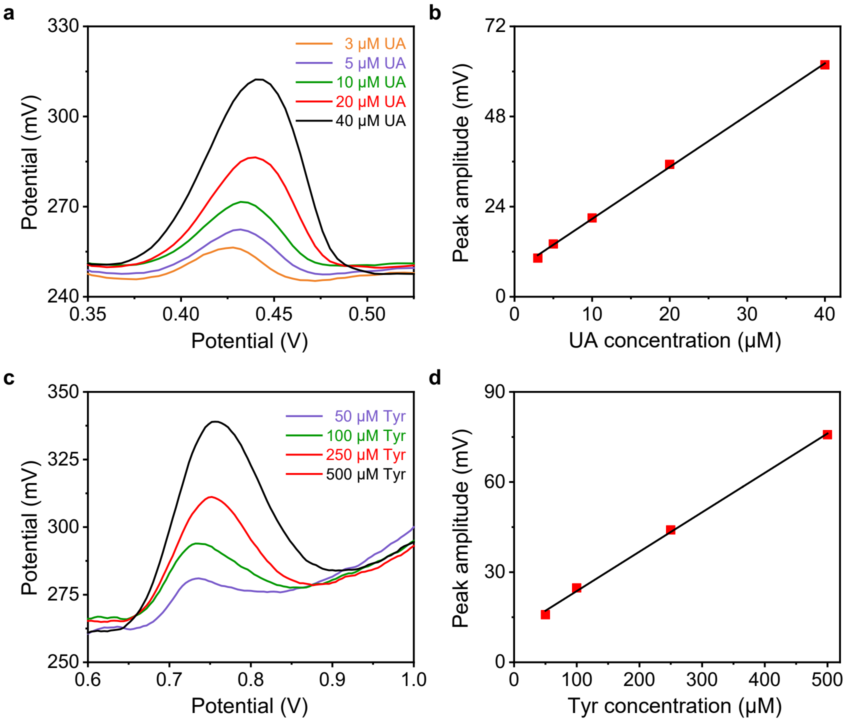

Supplementary Fig. 16. Characterization and calibration of LEG-CS using the FPCB. a,**b**, DPV curves in ABS solutions containing varied UA concentrations (**a**) their corresponding calibration curve (**b**). **c**,**d**, DPV curves of Tyr in ABS solutions containing varied Tyr concentrations (**c**) and their corresponding calibration curve (**d**). The experiment was repeated 5 times independently with similar results.

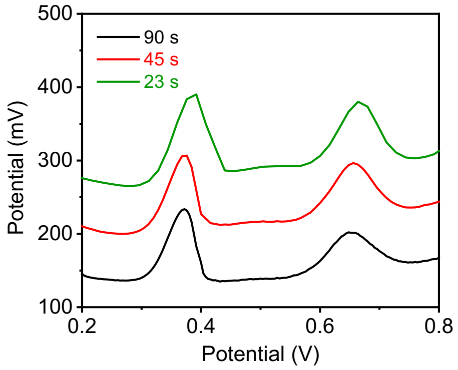

Supplementary Fig. 17. Control of the DPV scan cycle lengths by varying the scan steps. Varied incremental potentials (4, 8, and 16 mV) were used to achieve the scan cycle lengths of 90, 45, 23 seconds. Conditions, 50 μM UA and 250 μM Tyr. The experiment was repeated 5 times independently with similar results.

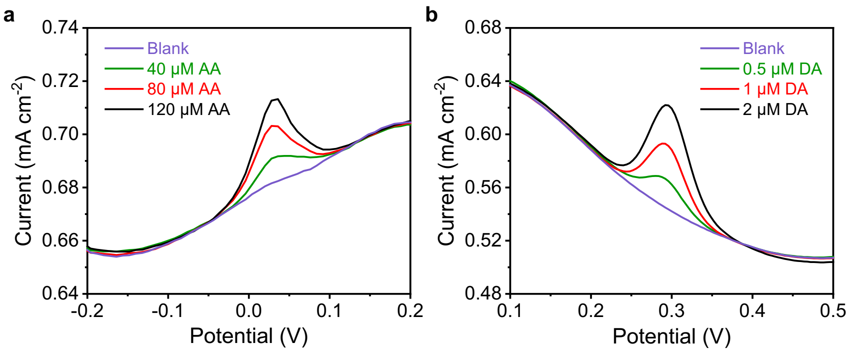

Supplementary Fig. 18. Sensor performance for detection of ultra-low levels of other electroactive compounds. a,**b**, the LEG electrodes show excellent sensitivity to AA (40, 80, and 120 μM) (**a**) and DA (0.5, 1, and 2 μM) (**b**). A commercial Ag/AgCl was used as the reference electrode. The experiment was repeated 5 times independently with similar results.

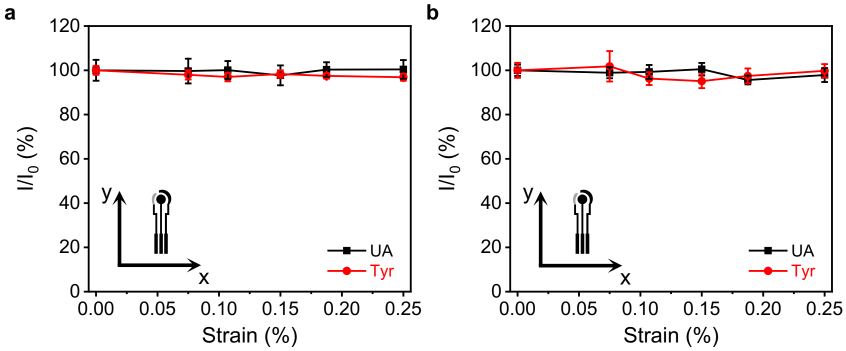

Supplementary Fig. 19. Stability of the LEG-CS during the bending tests. a,**b**, The long term stability of an LEG-based sensor during the bending test. 0–0.25 % strains were applied for both x (**a**) and y (**b**) axis. I and I_0 represent the current amplitude of the DPV plot during the bending, and the average current amplitude without bending, respectively. The error bars represent the standard deviation of 10 measurements, the mean of the 10 measurements is measure of the centre. Conditions, 50 μM UA and 100 μM Tyr.

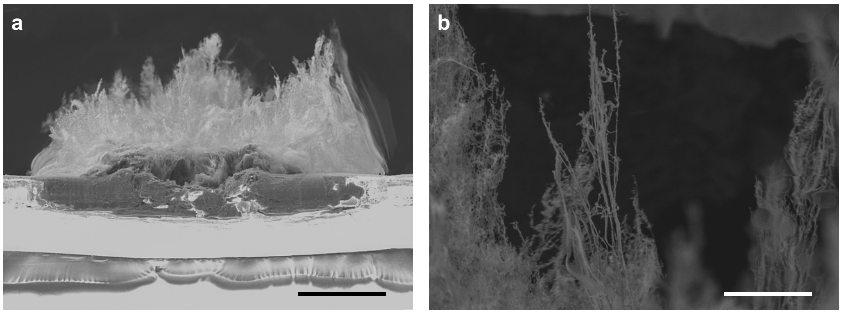

Supplementary Fig. 20. Porous fiber-like graphene structure for strain sensing. a, Cross-section SEM image of the fiber-like LEG. Scale bar, 100 µm. **b**, Magnified view of the fiber-like LEG structure. Scale bar, 10 µm.

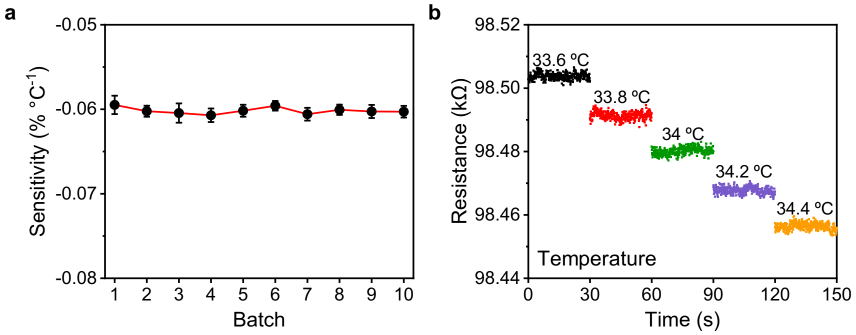

Supplementary Fig. 21. Characterization of the LEG-based temperature sensors. a, Batch to batch variation of the LEG-based temperature sensor performance (10 batches). Error bars represent the standard deviations of 10 measurements from a temperature sensor; the mean of the 10 measurements is measure of the centre. **b**, The response of an LEG-based temperature sensor to small temperature changes. The experiment was repeated 5 times independently with similar results.

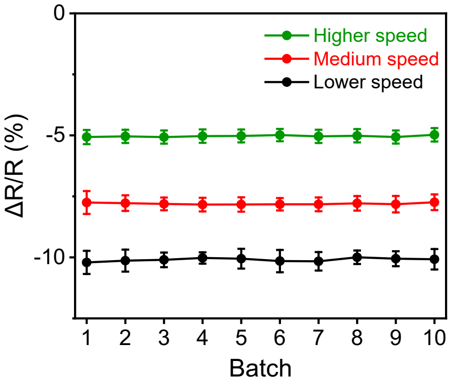

Supplementary Fig. 22. Batch to batch variation of the LEG-based strain sensors prepared with varied laser scanning speeds. Error bars represent the standard deviations of 10 measurements from a strain sensor under 0.25% strain; the mean of the 10 measurements is the center of measure.

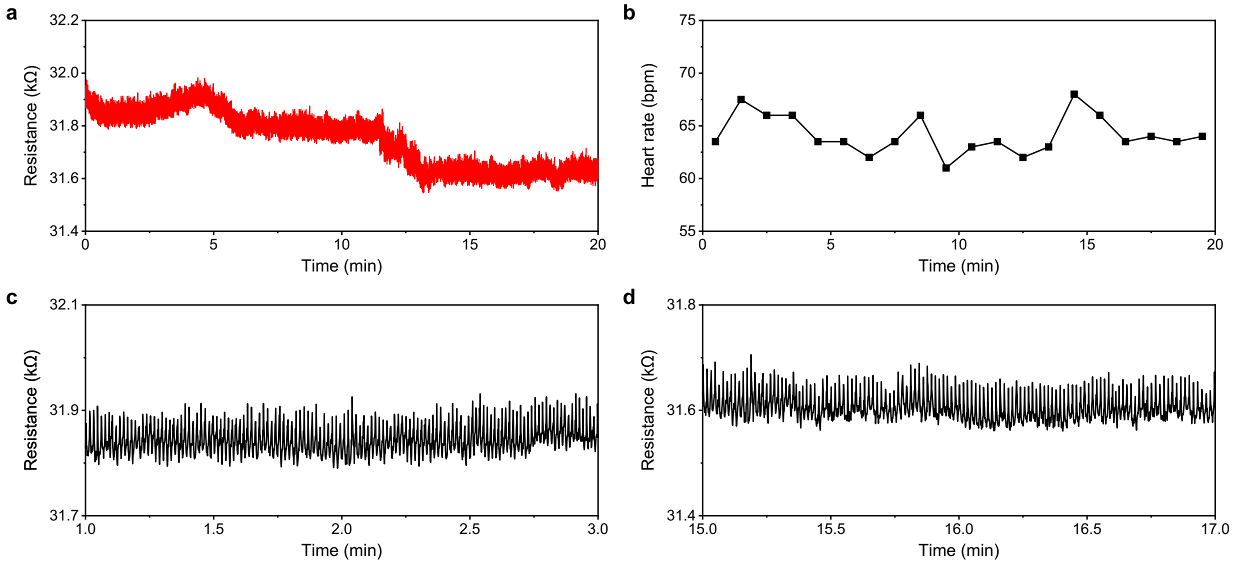

Supplementary Fig. 23. Heart rate (HR) monitoring using an LEG-based strain sensor. a,**b**, The resistive response of an LEG-based strain sensor (**a**) and extracted heart rate information (**b**) during long term continuous pulse monitoring on a healthy subject. **c**,**d**, The resistive responses of the LEG-based strain sensor at 1–3 minutes and at 15–17 minutes during this test.

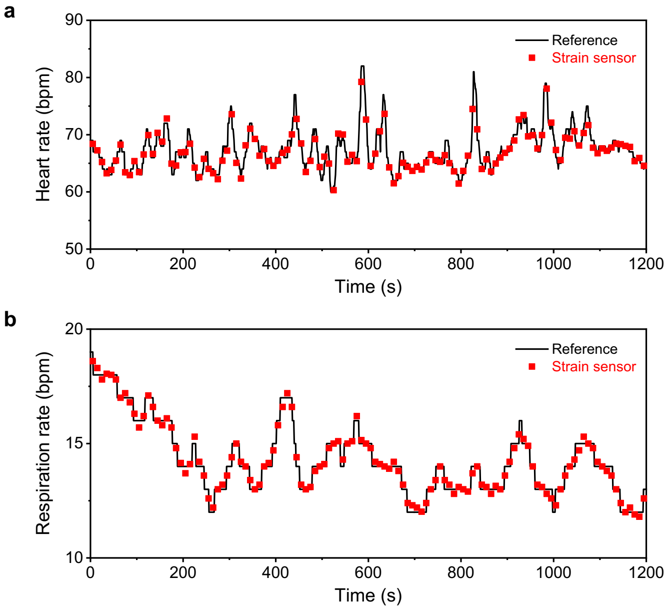

Supplementary Fig. 24. On-body sensor validation using an FDA-approved vital sign monitor during one session. a, Validation of an LEG-PS for heart rate monitoring using an FDA-approved heart rate monitor. **b**, Validation of an LEG-PS for respiration rate monitoring using an FDA-approved respiration rate monitor.

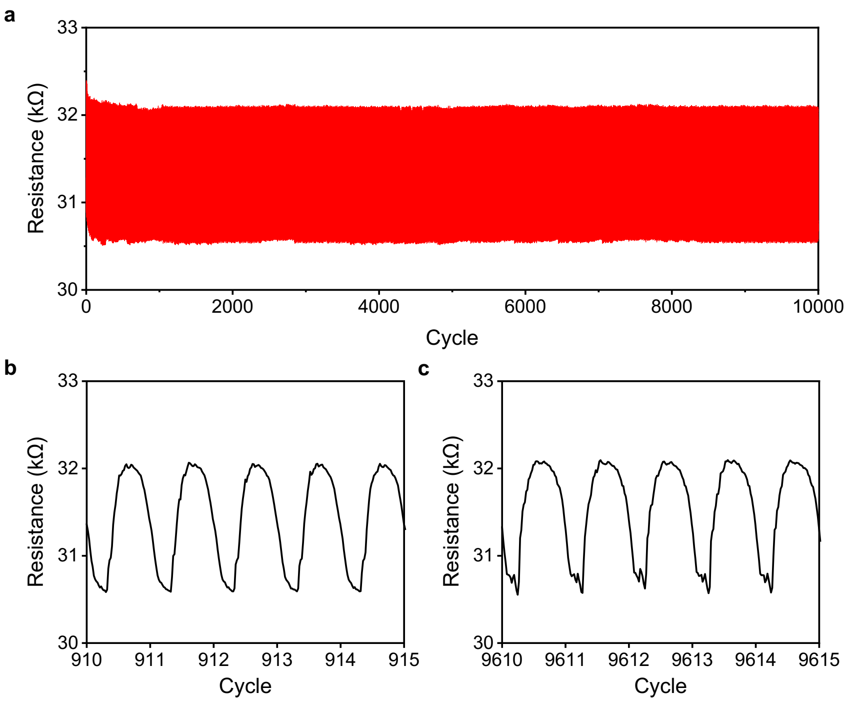

Supplementary Fig. 25. The long term stability of the LEG-based strain sensor over one bending session. a, The measurement was performed during a bending test of a strain sensor (10,000 cycles with strains alternated between 0% and 0.1%). **b**,**c**, The resistive sensor response during 910–915 cycles (**b**) and 9610–9615 cycles (**c**) of bending.

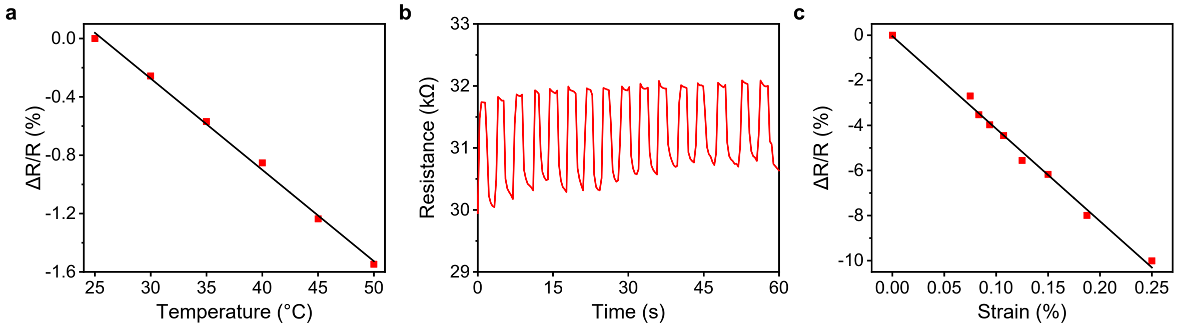

Supplementary Fig. 26. Characterization and calibration of the temperature and strain sensors using the FPCB. a, Calibration curve for the temperature sensor. **b**,**c**, Characterization in response to pulsed strains (**b**) and the calibration plot of the strain sensor (**c**). Throughout the figure, the experiments were repeated 3 times independently and similar results were obtained.

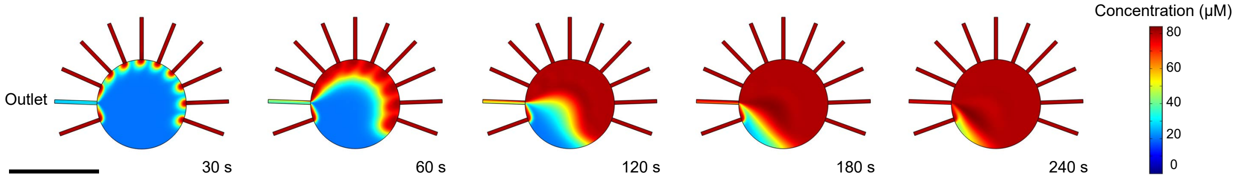

Supplementary Fig. 27. The numerical simulation showing the fluidic dynamics in the reservoir of the lab-on-skin sensor patch. The dimension used here are based on actual sensor design used in this work. Scale bar, 5 mm.

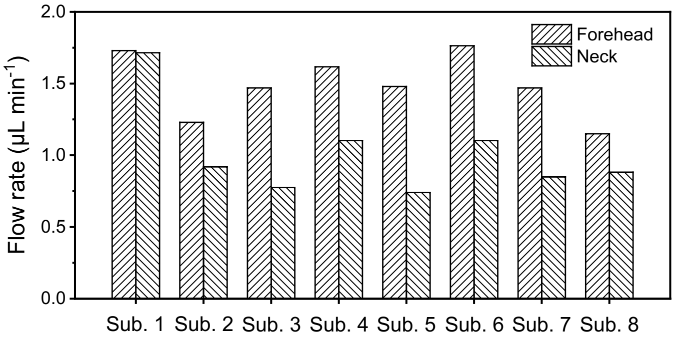

Supplementary Fig. 28. Inferred sweat rates from different locations of eight healthy subjects obtained via optical image analysis. Sub., subject.

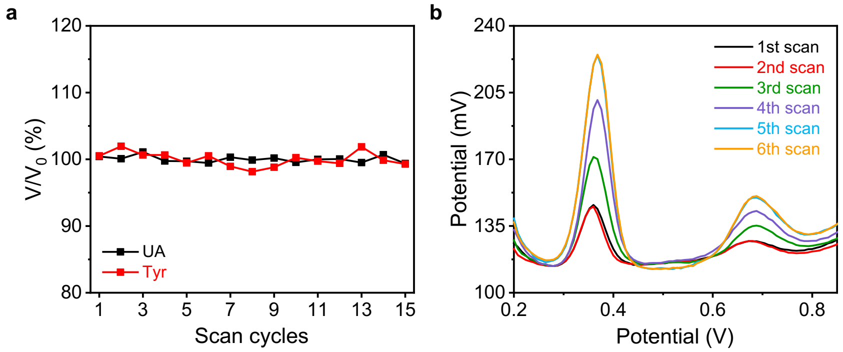

Supplementary Fig. 29. Characterization of the dynamics of the continuous microfluidic sensing. a, Stable peak amplitudes of twelve successive DPV scans in a solution containing 80 μM UA and 200 μM Tyr with a fixed flow rate of 1 μL min^{-1}. **b**, Dynamic DPV response of the microfluidic sensing when the inflow solution was switched from 20 μM UA and 50 μM Tyr to 80 μM UA and 200 μM Tyr with a fixed flow rate of 1 μL min^{-1}. A DPV scan was performed every minute (with a scan step of 8 mV and a scan cycle of 45 seconds). Throughout the figure, the experiments were repeated 3 times independently and similar results were obtained.

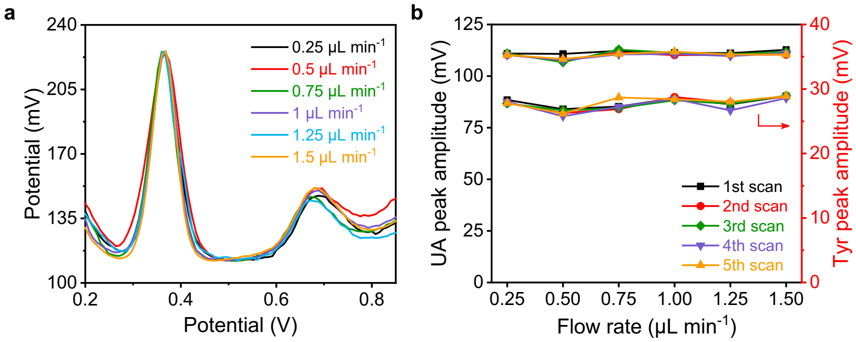

Supplementary Fig. 30. Characterization of continuous microfluidic sensing performance under different flow rates. a, The DPV plots of an LEG-CS for UA and Tyr sensing at different flow rates (from 0.25 to 1.5 μL min^{-1}). **b**, The peak amplitudes of UA and Tyr in 5 successive DPV scans (2.5 minutes per scan with a 45-s scan cycle length) with different flow rates (from 0.25 to 1.5 μL min^{-1}). Conditions, 80 μM UA and 200 μM Tyr. Throughout the figure, the experiments were repeated 3 times independently and similar results were obtained.

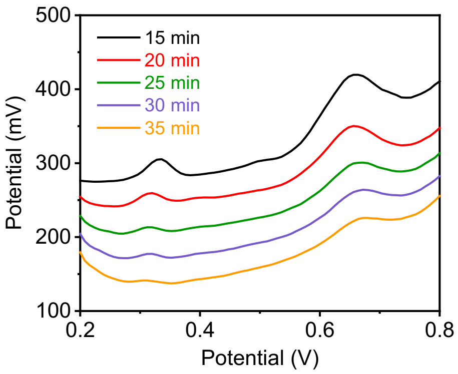

Supplementary Fig. 31. The DPV plots obtained by the sensor patch from a healthy subject's neck during the cycling exercise, in one biking session. Conditions, same as **Fig. 5b**.

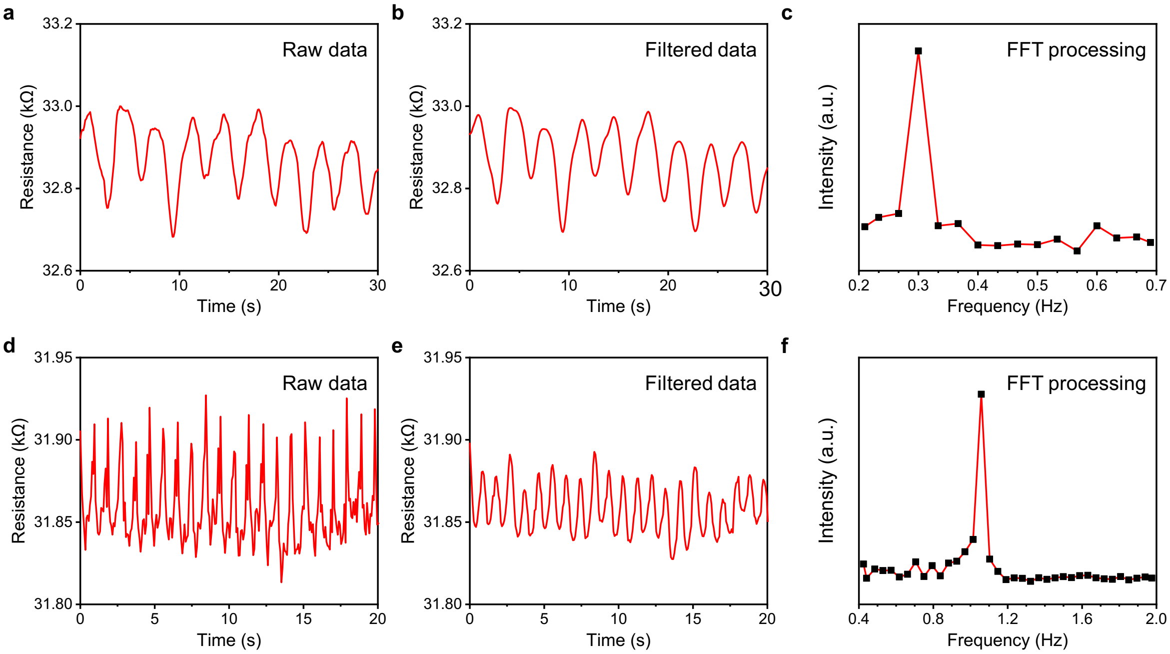

Supplementary Fig. 32. Data processing of the strain sensor involving data filtering and fast Fourier transform (FFT) to obtain the heart rate (HR) and respiration rate (RR) values. a–c, An example of the raw data (**a**), filtered data (**b**), and FFT extracted frequency data (**c**) toward RR monitoring. The raw data was collected by a strain sensor from a healthy subject. **d–f**, An example of the raw data (**d**), filtered data (**e**), and FFT extracted frequency data (**f**) toward HR monitoring. HR and RR values were obtained from the frequencies that had highest intensity in the given periods. The raw data was collected by a strain sensor from a healthy subject.

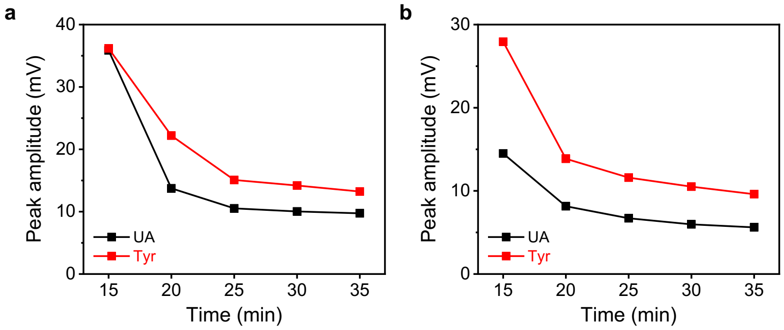

Supplementary Fig. 33. The peak amplitude of DPV curves in Fig. 5c,d obtained during the on-body UA and Tyr measurement from the neck (a) and the forehead (b) of a healthy subject during one biking session.

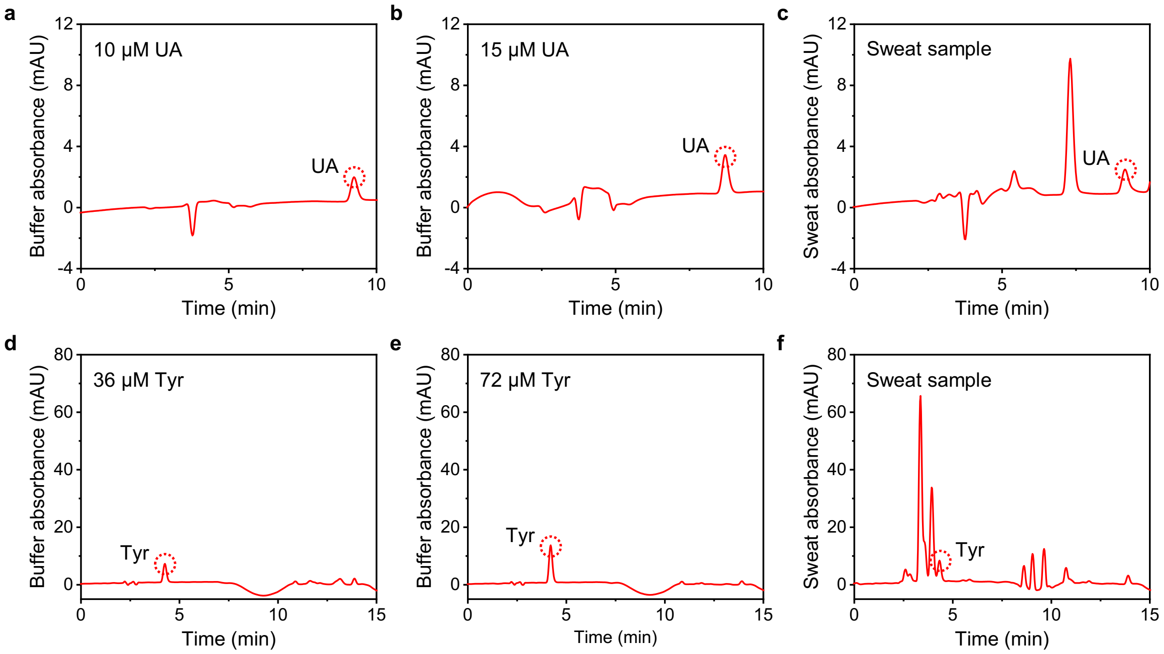

Supplementary Fig. 34. HPLC analyses of the UA and Tyr in sweat. The experiments were repeated 3 times independently and similar results were obtained.

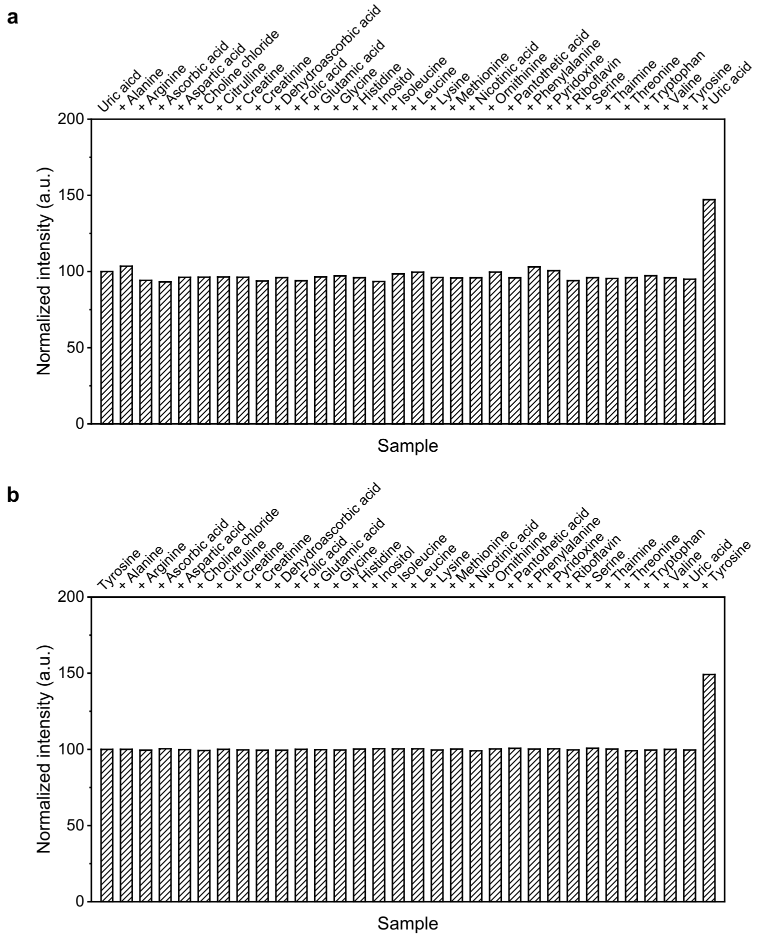

Supplementary Fig. 35. Selectivity of HPLC analyses of the UA (a) and Tyr (b) over common sweat analytes. The concentrations of the initial UA/Tyr and added other analytes are based on **Supplementary Table 2**. UA and Tyr levels were increased by 50% in the end for **a** and **b**, respectively. Throughout this figure, the experiments were repeated 3 times independently and similar results were obtained.

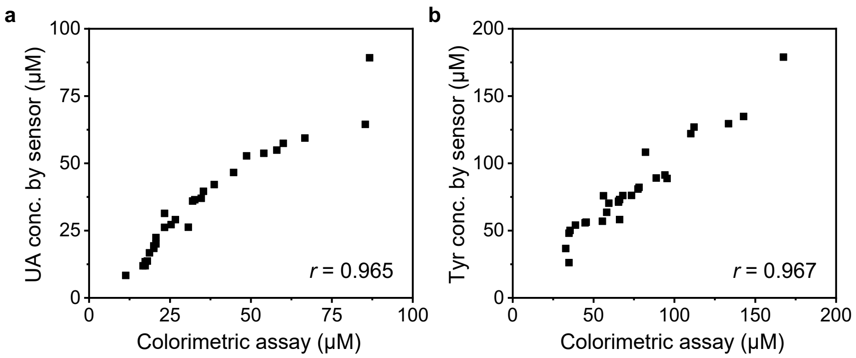

Supplementary Fig. 36. Validation of the accuracy of the LEG-CS for UA (a) and Tyr (b) sensing using colorimetric assay kits. The data are based on 28 sweat samples collected from the healthy subjects. UA and Tyr concentrations by the sensor were obtained from the sensor reading and the linear fitting in **Fig. 5e**,**f**. The Pearson correlation coefficient was acquired through linear regression.

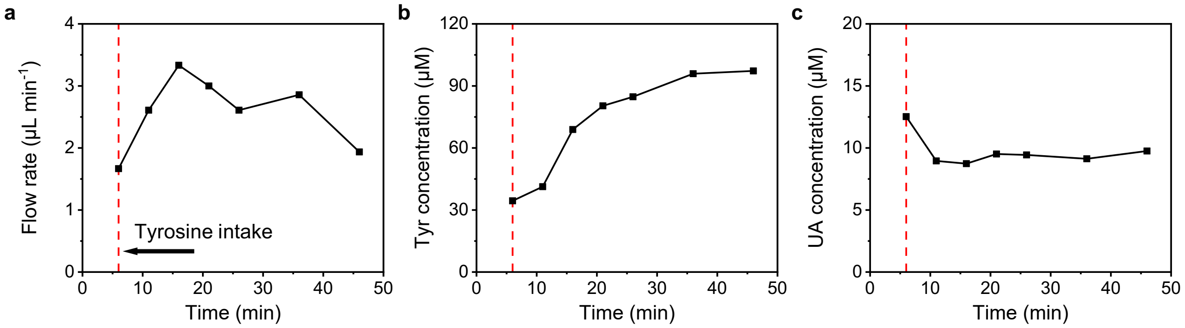

Supplementary Fig. 37. Dynamic Tyr monitoring using the sensor patch after Tyr supplementation. The experiment was performed on a healthy subject over one iontophoresis-induced sweat secretion process. The experiment was repeated twice independently with similar results.

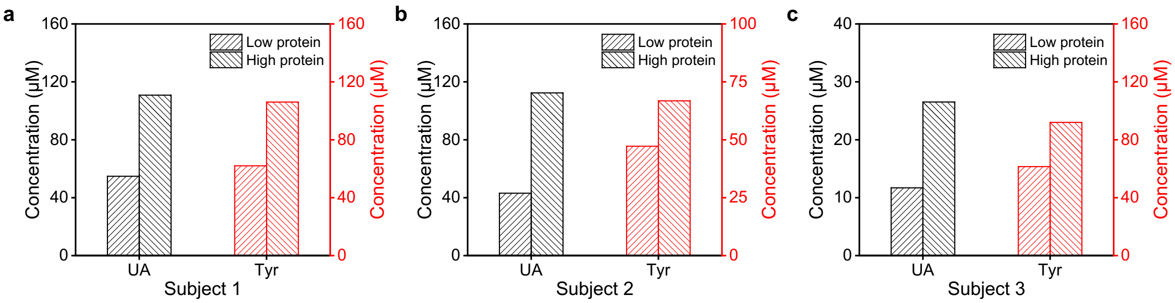

Supplementary Fig. 38. The influence of high and low protein intakes on sweat UA and Tyr.

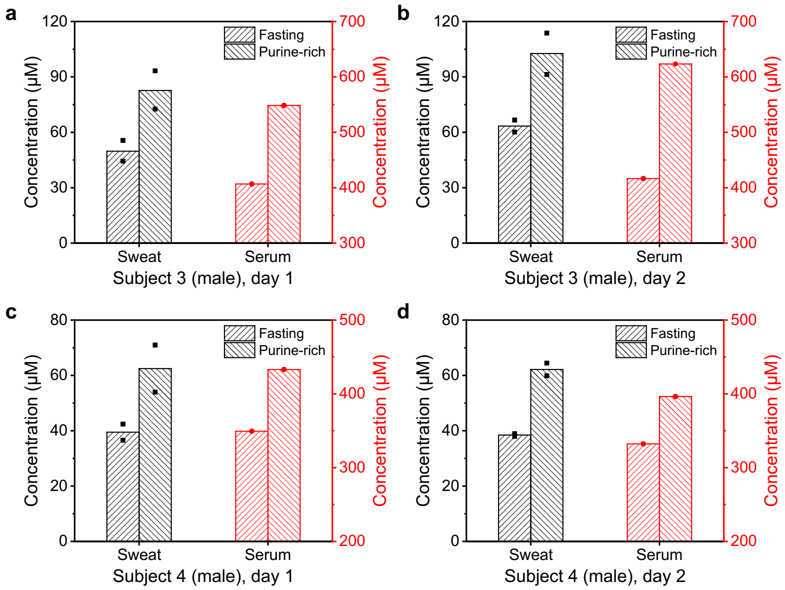

Supplementary Fig. 39. Investigation of the sweat and serum UA levels using a purine-rich diet challenge. UA levels in sweat and serum of two heathy subjects under fasting condition, and after a purine-rich diet on two different days. Measure of the center in **a–d** is the mean value of the first two successive measurements.

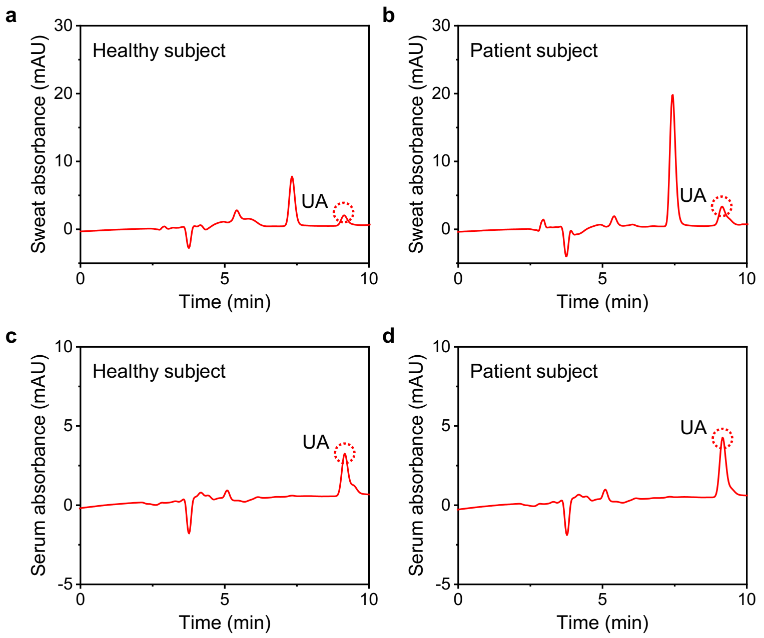

Supplementary Fig. 40. HPLC analyses of the sweat (a,b) and serum (c,d) UA levels of a healthy subject (a,c) and a patient with gout (b,d). The experiment was repeated 3 times independently with similar results.

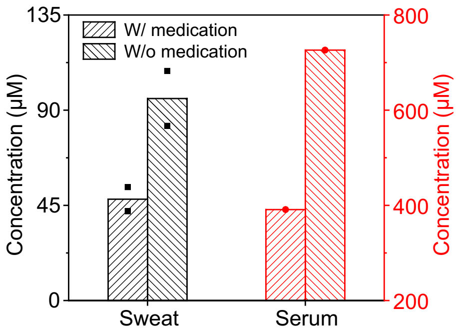

Supplementary Fig. 41. The influence of urate-lowering medication (allopurinol) on the sweat and serum UA levels. The sweat and blood tests were performed on the same gout patient on two days: on one day the patient received urate-lowering medication 2 hours before the test, and on the other day the patient did not take medication 24 hours before the test. The center of measure is the mean value of the first two successive measurements from one patient.

Supplementary Table 1. Optimization of the LEG-CS with different laser parameters.

Electrode #	Power (%)	Speed (%)	PPI	UA Peak (mA cm^{-2})	Tyr Peak (mA cm^{-2})
1	6.3	5.5	1000	0.142	0.061
2	6	5	1000	0.003	0
3	6	6	1000	0.091	0.035
4	6	7	1000	0.113	0.029
5	6	8	1000	0.05	0.013
6	5.5	5	1000	0	0
7	6.5	5	1000	0.132	0.043
8	7.5	5	1000	0.101	0.032
9	6	5	250	0.138	0.045
10	6	5	500	0.115	0.049
11	6	5	750	0.1	0.033
12	6	5	1000	0.131	0.031

Supplementary Table 2. Sweat analytes and their concentrations used for the selectivity studies. The values were chosen based on the mean physiological levels of the analytes[46].

Number	Constituents	Concentration (μM)	Number	Constituents	Concentration (μM)
1	Alanine	360	17	Lysine	150
2	Arginine	780	18	Methionine	50
3	Ascorbic acid	10	19	Nicotinic acid	50
4	Aspartic acid	340	20	Ornithine	150
5	Choline chloride	50	21	Pantothetic acid	50
6	Citrulline	400	22	Phenylalanine	130
7	Creatine	15	23	Pyridoxine	0.01
8	Creatinine	84	24	Riboflavin	50
9	Dehydroascorbic acid	11	25	Serine	50
10	Folic acid	50	26	Thiamine	50
11	Glutamic acid	370	27	Threonine	450
12	Glycine	390	28	Tryptophan	55
13	Histidine	520	29	Tyrosine	170
14	Inositol	1.6	30	Uric acid	60
15	Isoleucine	16	31	Valine	250
16	Leucine	210			

Supplementary Table 3. UA HPLC gradient method.

Eluent A	Eluent B	Flow rate	Time (min)	Percentage eluent B (%)
0.1% Formic acid	Acetonitrile 100%	0.34 mL min^{-1}	0	0
			6	0
			6.2	100
			7.5	100
			7.9	0
			15	0

Supplementary Table 4. Tyr HPLC gradient method.

Eluent A	Eluent B	Flow rate	Time (min)	Percentage eluent B (%)
50 mM KH_2PO_4-H_3PO_4 buffer pH 3.0	Methanol 100%	0.425 mL min^{-1}	0	9.1
			4	9.1
			8	80
			12	80
			15	9.1
			20	9.1

Supplementary Note 1. The selectivity of the LEG-CS for sweat UA and Tyr sensing

Current wearable electrochemical sweat sensors are primarily focused on a limited number of electrolytes (e.g., Na^+, K^+, Cl^-) and metabolites (e.g., lactate and glucose) at high concentrations (usually at mM levels) monitored *via* ion-selective sensors or enzymatic electrodes; biosensors based on bioreceptors (e.g., antibodies) could be highly sensitive, but usually require multiple washing steps and detection in standard buffer or redox solutions in order to transduce the bioaffinity interactions.

The approach we utilize here for continuous monitoring of UA and Tyr is based on their selective oxidation reaction at a specific potential. The selectivity is based on the oxidation peak position for the LEG-CS. We evaluate here the selectivity of the LEG-CS over the common amino acids, vitamins and other potential interfering chemicals at physiological relevant concentrations in human sweat listed in **Supplementary Table 2**. Our electrochemical sensing data in **Supplementary Figs. 11** and **12** show that the physiological level sweat analytes have minimal influence on the detection of UA and Tyr using the LEG-CS.

There are few electroactive molecules reported to be present in human sweat with comparable concentrations with UA and Tyr. Dopamine is a well-known electroactive neurotransmitter present at high concentration in cerebrospinal fluid. Our data in **Fig. 2i** shows that at the same conditions, the dopamine oxidation peak appears at a more negative potential than UA and doesn't affect the UA monitoring. In fact, to our knowledge, there is no literature report on the presence of dopamine in human sweat. Another electroactive molecule tryptophan has a close oxidation peak position to Tyr. However, tryptophan is present at a much lower concentration compared to Tyr. Our selectivity study (**Supplementary Fig. 13**) shows that physiologically relevant concentrations of tryptophan do not significantly affect our Tyr measurement.

As pH is usually a key factor that could influence electrochemical sweat sensor performance, we try to evaluate here the influence of pH on the sensor performance in artificial sweat (with pH values adjusted by varying lactic acid as lactic acid is the main contributing factors for sweat pH). Considering the normal sweat pH range in the literature and from our human subjects (pH ranges from 4 to 6), the dependence of the chemical sensor performance in artificial sweat with pHs between 4 to 6 was examined. Our results in **Supplementary Fig. 14** show that, although the oxidation peak positions slightly shift under different pHs, the peak amplitudes of UA and Tyr sensing remain stable in the range of pH 4 to pH 6. Considering that we are essentially measuring the peak heights, the influence of the pH is small to our sensors. Moreover, it is worth noting that the variations of pH values of an individual's sweat at different time points during biking session and at different biking sessions are small.

To further validate the accuracy and selectivity of the LEG-CS, the sensor readings in human sweat samples have been validated with two current gold standards – high performance liquid chromatography (HPLC) (**Fig. 5e,f** and **Supplementary Fig. 35**) and commercial colorimetric assay kits (**Supplementary Fig. 36**). Very high linear coefficients (0.963 and 0.965 for UA and Tyr with HPLC, 0.965 and 0.967 for UA and Tyr with the commercial colorimetric assays) were found, revealing the great reliability and accuracy of our sensor technology toward sweat UA and Tyr sensing.